Influence of phase angle and dead volume on gamma-type Stirling engine power using CFD simulation

Alfarawi, Suliman; Al-Dadah, Raya; Mahmoud, Saad

DOI:
10.1016/j.enconman.2016.07.016

Document Version
Peer reviewed version

Citation for published version (Harvard):
Alfarawi, S, Al-Dadah, R & Mahmoud, S 2016, 'Influence of phase angle and dead volume on gamma-type Stirling engine power using CFD simulation', *Energy Conversion and Management*, vol. 124, pp. 130-140. https://doi.org/10.1016/j.enconman.2016.07.016

INFLUENCE OF PHASE ANGLE AND DEAD VOLUME ON GAMMA-TYPE STIRLING ENGINE POWER USING CFD SIMULATION

S. Alfarawi[1], R. AL-Dadah[1], S. Mahmoud[1]

[1]Department of Mechanical Engineering, University of Birmingham, Edgbaston, B15 2TT, UK

Abstract

This work presents the development and validation of computational fluid dynamics (CFD) model of 500 Watts gamma-type Stirling engine prototype to highlight the effects posed by phase angle and dead volume variations on engine performance. The model is based on a realistic Local Thermal Non-Equilibrium (LTNE) approach for porous domains in the engine (cooler and regenerator). The simulation results showed an acceptable degree of accuracy of 9% and 5%, respectively when comparing with experimental results in predicting the indicated and cooling powers at different heating temperatures. It is found that the maximum indicated power is achieved at a phase angle of 105° rather than at the common phase angle of 90°. The dead volume (connecting pipe) is observed to pose negative effects on engine indicated power and therefore, an optimum value of pipe diameter exists.

Keywords: CFD, Phase angle, Stirling Engine, dead volume.

Nomenclature

2D	Two dimensional	r	Crank radius, mm
a_{fs}	Solid surface area per unit volume, 1/m	Re	Reynolds number
CFD	Computational fluid dynamics	T	Gas phase temperature, °C
C_p	Gas heat capacity, J/kg. K	T_s	Solid phase temperature, °C
C_{ps}	Solid heat capacity, J/kg. K	$\boldsymbol{u}$	Velocity vector, m/s
d_w	Mesh wire diameter, µm	X_c	Power piston displacement, m
d_h	Hydraulic diameter, m	X_e	Displacer piston displacement, m
f	Friction factor	*Greek letters*	
K	Permeability, m^2	β_F	Forchheimer drag coefficient, kg/m^4
k	Gas thermal conductivity, W/m. K	λ_c	Crank radius to compression connecting rod ratio
k_s	Solid thermal conductivity, W/m. K	λ_e	Crank radius to expansion connecting rod ratio
$\overline{\overline{k_e}}$	Equivalent thermal conductivity, W/m. K	θ	Crank angle, rad
Nu	Nusselt number	ρ	Gas density, kg/m^3
p	Instantaneous gas pressure, Pa	ρ_s	Solid density, kg/m^3
P_e	Peclet number	μ	Gas dynamic viscosity, Pa. s
R	Gas constant, J/kg. K	ε	Porosity

1. Introduction

Alternative sources of energy are being sought to preserve fossil fuels as well as to reduce the greenhouse effects. In this regard, renewable energy resources (such as biomass, solar, geothermal and wind energy) are deemed to be the promising solution in as much as they are clean, efficient, and sustainable [1]. The Stirling engine is an externally heated engine. It is thermally regenerative, simple in construction, virtually quiet, safe in operation, and intrinsically flexible to adopt any heat source such as solar, biomass, geothermal energy or even an industrial waste [2]. Ideally, Stirling engines work on a highly efficient thermodynamic cycle. The gas inside the engine undergoes four processes; two isothermal heat-exchange processes (expansion and compression) and two isochoric heat-exchange processes (heating and cooling). However, the real cycle is considerably penalized due to the irreversibility and non-ideality of transport mechanisms occurring inside the different components of the engine. The regenerator is a key component of the engine; it is an internal heat exchanger that acts as a thermal sponge that absorbs and releases heat during the cycle, thus, enhancing engine power and efficiency. The heat being absorbed and restored to the gas in the regenerator during one cycle is typically four times the heat that passes through the heater during one cycle [3]. Without a regenerator, such an engine requires a heater with five times the amount of heat needed to generate the same power it did with a regenerator. The conventional regenerator types adopted in Stirling engines are wire mesh or random fibre. Some advantageous features exist in these types such as; high convective heat transfer between the solid and the gas due to the extended surface area of wires and this is similar to a cross flow over repeated cylinder-shaped wires and low axial conduction in flow direction. However, the disadvantage of this type of regenerator is the high flow friction resulting from flow separation, eddies associated with stagnation areas that can degrade the engine performance. The regenerator has to have several features for better performance that might be contradicting and this requires a great effort for designers and developers to find the optimum configuration based on; minimum pressure drop, maximum convective heat transfer and minimum axial conduction in flow direction [4]. There have been numerous numerical models in open literature to analyse and optimize Stirling engines. In their hierarchal order, they are classified as zeroth-, first-, second-, third- and forth-order models. The first four models are ascending in their complexity and accuracy. However, the effects caused by the geometrical variation can't be taken into account by these models. A detailed overview of these models can be found in [5]. The adoption of fourth-order analysis or namely computational fluid dynamics (CFD) analysis can return accurate results. However, this approach is quite challenging and computationally expensive to model the engine as a whole. In terms of full engine CFD modelling, the thermal equilibrium used in porous media models for modelling the regenerator is believed to be a poor assumption in oscillating flow environment since several degrees of temperature difference between gas and

solid matrix are reported [6]. The Navier-Stokes equations are either for laminar or turbulent regimes contrasting with the actual flow situation in Stirling environment and hence transition from laminar to turbulent can occur from one spatial location to another over the cycle based on the published results of oscillating flow rig testing. Therefore, more understanding of flow physics is still required [7]. The deformation of engine domains due to pistons movement as a result of gas compression and expansion needs to be handled through a complex algorithm to support moving (dynamic) meshes during the simulation. The time stepping in transient analysis plays a crucial role on convergence and accuracy of the simulation. Movements of the pistons until reaching the dead points, where the mesh is densely compressed, may require smaller time steps for better convergence and hence adaptive time stepping can be a good strategy to return results more accurately. Therefore, using this approach needs more sophisticated codes, and sometime manual tuning is required, in order to return more reasonable and accurate results. There have been fewer studies on using CFD approach than other analysis methods for modelling Stirling engine in general and for modelling gamma-type in particular.

Bert et al. [8] proposed a three-zone finite-time thermodynamic model to simulate and optimize gamma-type Stirling engine with a nominal power of 1kWe. Effects of speed, gas type, hot end temperature and filling pressure on engine performance were investigated. The pistons kinematics were optimized using particle swarm optimization (PSO) for maximum power. Their results showed that in the optimized crank-connecting rod system, the phase angle varies from 90° at the beginning of the cycle and 100° at the maximum position of each piston.

Chen et al. [9] constructed and tested a twin power piston gamma-type Stirling engine. The engine was incorporated with a moving regenerator housed inside its displacer and filled with a woven-screen material. The effects of different regenerator parameters on engine performance, including regenerator material, wire diameter, filling factor and stacking arrangements, were investigated. According to their results, copper material was found superior to stainless steel on engine performance at the tested conditions and optimum filling factor was proposed.

Hooshang et al. [10] proposed a model for gamma-type Stirling engine optimization based on neural network concepts. The thermodynamic code based on third-order analysis was used to produce a dataset to recognise the relationship between inputs and outputs using the neural network and to search for optimum design parameters. The results showed that engine power and efficiency can be optimized to 878 W and 13.21% compared to the base case of 500 W and 8.5%.

Hachem et al. [11] developed a numerical model, based on classical quasi-steady approach, to optimize gamma-type Stirling engine. Their results showed that the maximum losses were recorded in the regenerator including viscous,

conduction and imperfection losses. The effect of key operational parameters, such as engine speed, hot end temperature and charge pressure on engine performance were investigated and they found that the engine speed can cause a conflict of thermal losses mechanisms. Increasing initial filling pressure and hot end temperature were the two influential parameters on the increase of engine brake power.

Araoz et al. [12] developed a thermodynamic model based on second-order analysis to simulate gamma-type Stirling engine. The forced work and mechanical efficiency, based on Senft theory, were considered to predict engine shaft power. According to their results, they found that the engine low power output was attributed to the reduced mechanical efficiency of the system. The dynamics of volume variation and drive mechanism were suggested for further improvements to increase the engine shaft power.

Gheith et al. [13] conducted an experimental investigation on the optimum regenerator matrix material and porosity for gamma-type Stirling engine. Different materials were tested including stainless steel, copper, aluminium and Monel 400. The results showed that stainless steel matrix with 85% porosity is the best configuration to maximize engine performance.

Li et al. [14] proposed a coupled finite speed and isothermal models to analyse a solar-powered gamma-type Stirling engine. A filling material in regenerator gap was not considered in this LTD Stirling engine. Different loss mechanisms affecting the engine performance were considered. They found that the key loss mechanisms are the regenerator gap heat loss and the work loss due to gas leakage through piston/ cylinder walls. Some engine improvements; using isolating material for displacer and cylinder walls and reducing the clearance leakage, were proposed.

Mahkamov [15], performed a second-order and 3D CFD analysis on a gamma-type Stirling engine prototype to enhance its power. The CFD results revealed that power reduction was attributed to the high level of hydraulic losses in the regenerator, and the entrapment of the gas in the pipe connecting the two parts of the compression space and to its large dead volume. A further improvement in the engine design was only viable by adopting this multi-dimension approach within an acceptable range of accuracy, 18% when compared to experimental results.

Chen et al. [16] developed a 3D CFD code for twin power piston gamma-type Stirling engine. Several time-dependent parameters such as temperature, heat input, heat output and engine power were calculated. The results showed that impingement is the key mechanism for heat transfer in expansion and compression champers with non-uniform temperature distribution across the engine volume.

Chen et al. [17] developed an in-house CFD model to simulate gamma-type LTD Stirling engine. Several geometrical and operational parameters effect including pistons strokes, radius of power piston, hot and cold temperature difference and speed, on engine performance were investigated. It was found that the increase in power piston radius strongly affected engine performance due to the increased compression ratio.

Hooshang et al. [18] developed a combined dynamic-thermodynamic model for gamma-type Stirling engine simulation. The dynamic response based on engine kinematic relations were linked to 1D third-order thermodynamic analysis code to evaluate the instant variation of engine parameters such as velocity, density, convective heat transfer and temperature in each engine chamber. Their code was able to predict engine power and rejected heat rate compared to experiment within maximum deviation of 11% and 18%, respectively.

CFD modelling as a whole of the current high temperature differential (HTD) Stirling engine prototype (ST05CNC) has not been reported yet in literature. All previous studies [8,10,18] on the same engine configuration were based on second- and third-order models with a prediction accuracy ranging from 11-18%. Usually, such models are tuned to fit experimental data due to their dependency on empirical coefficients such as heat transfer leading to limited application. In contrast, CFD approach can be applied to any Stirling engine type as all variation of a parameter is inherently embedded in the the Navier-Stokes equations. This work aims to develop and validate a comprehensive CFD model, based on a commercially available software (COMSOL Multiphysics 5.2) to simulate the gamma-type Stirling engine prototype (ST05 CNC) described below. The developed model was used to investigate the effect of phase angle and connecting pipe dead volume on engine indicated and cooling powers and hence the optimum values were proposed.

2. Engine Description

The engine is a gamma-type that was first designed by Dieter Viebach in 1992 in Germany to promote microgeneration with biomass fuels and since then was opened for research development [19]. The engine, shown in Fig. 1, is composed of power and displacer pistons with 90° phase angle, and three heat exchangers (heater, cooler and regenerator). The heater is comprised of 20 tubes made of stainless steel with 6mm inner diameter each. The cooler is an aluminium finned type heat exchanger (144 internal fins, 1mm by 10mm cross sectional area each) with a volumetric porosity of 39.5%. the regenerator is fitted with a stainless steel random fibre of 31-micron wire diameter and 90% volumetric porosity. The engine is externally heated by an electric heater with a maximum capacity of 7KW. The expansion and compression spaces are connected via a 30 mm concentric-cooled pipe.

Meanwhile, the engine is cooled by a circuit of cooling water normally at 15°C. The engine is instrumented with eight k-type thermocouples fitted in different locations of the engine for local temperature measurements; compression space, cooling water inlet, cooling water outlet, cooler working gas, regenerator cold end, regenerator hot end, heater working gas and heater wall. A high-pressure sensor is fitted in the compression space, for instantaneous pressure measurements and the engine is coupled with dynamometer for brake power measurement. The engine operational details are summarized in table 1.

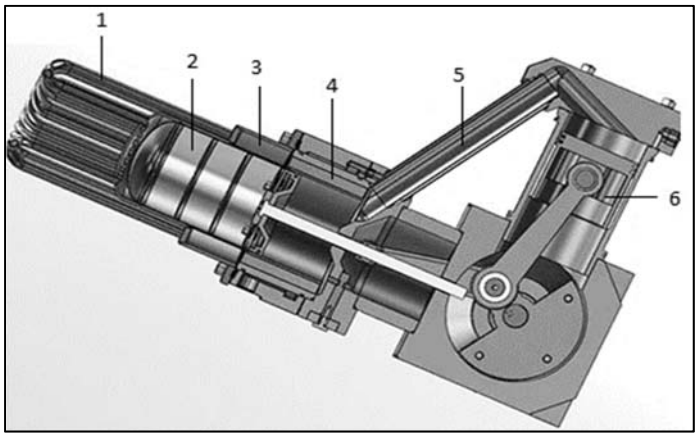

Fig. 1. Engine components: 1-Heater, 2-Displacer piston, 3-Regenerator, 4-Cooler, 5-Connecting pipe, 6-Power piston.

Table 1
Engine details.

Parameter	Value/description
Nominal rotational speed (rpm)	500
Stroke (mm)	75
Power piston bore (mm)	85
Displacer piston bore (mm)	96
Charge pressure (bar)	10
Working gas	N_2
Heater type	Tubular
Cooler type	Finned
Regenerator type	Random fibre
Wire diameter (Micron)	31
Porosity	0.9
Hot source temperature (°C)	650
Inlet water temperature (°C)	15
Water flow rate (L/min)	3.5
Water cooling power (kW)	2.3
Compression ratio	1.3

Uncertainty analysis is performed on engine measured parameters using the method presented in [20], and the results are tabulated in table 2. All sources of uncertainties may be linked to the inaccuracies of sensors, data acquisition system, junctions and electrical disturbance. The highest uncertainty, 2.87%, is recorded for cooling

power due to the relative uncertainties in measuring cooling water flow rate, inlet water cooling temperature, outlet water cooling temperature.

Table 2
Uncertainty analysis for measured parameters.

Device	Manufacturer	Measurement	Full Scale	Accuracy	Uncertainty
Thermocouple, k-type	Thermibel	Temperature	-200-250 °C	2.5 °C	1%
Thermocouple, k-type	Thermibel	Temperature	-200-1100 °C	10 °C	0.9%
High pressure sensor	Kistler	Pressure	0-20 bar	0.04 bar	0.2%
Incremental encoder	Lorenz	Velocity	0-1500 rpm	4.2rpm	0.28%
Flowmeter	Influx	Flowrate	1-10 L/min	0.25 L/min	2.5%
-	-	Indicated power	-	-	0.2%
-	-	Cooling power	-	-	2.87%

3. CFD Model

As the Stirling engine works by gas expansion and compression processes, the main physics in the engine are unsteady, transient, oscillating, laminar or turbulent, compressible flow and heat transfer. These sophisticated physics with geometrical effects can be handled within COMSOL Multiphysics environment [21]. The Arbitrary Lagrangian-Eulerian (ALE) method was used to handle the deformed geometry and the moving boundaries due to compression and expansion of the gas inside the engine. Meanwhile, compressible laminar Non-Isothermal flow is used to solve for fluid flow and heat transfer in the domains except the regenerator and the cooler (shown in Fig. 2). The regenerator and the cooler are modelled as porous media using Brinkman equation for fluid flow and the two Local Thermal Non-Equilibrium (LTNE) heat transfer equations for gas and solid phases.

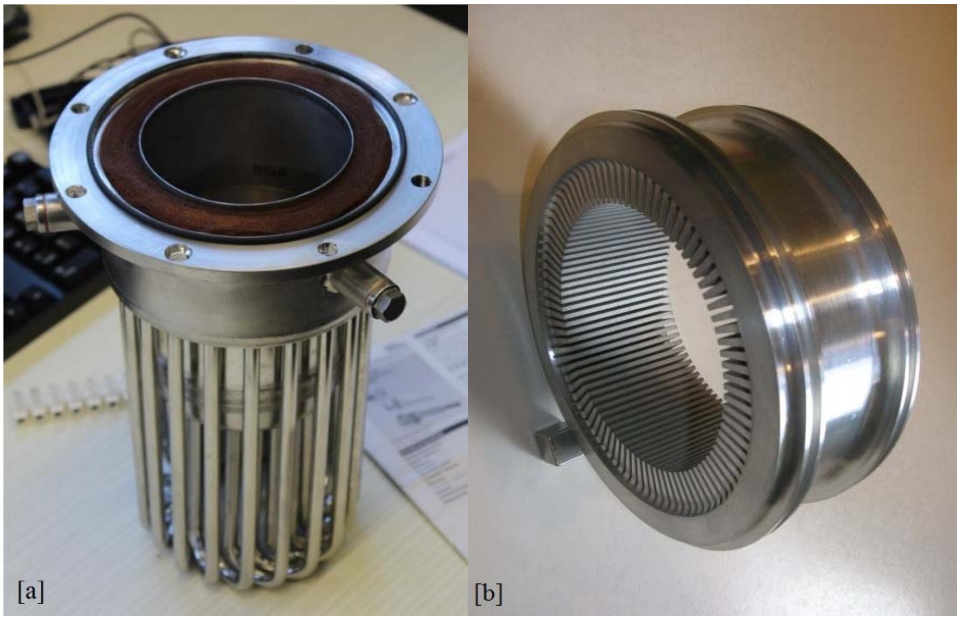

Fig. 2. Porous media domains, (a) regenerator, (b) cooler.

The governing equations in the porous domains, including continuity, momentum and energy equations for the gas phase [22] are:

$$\frac{\partial \rho}{\partial t} = \frac{\nabla.(\rho \boldsymbol{u})}{\varepsilon} \tag{1}$$

$$\frac{\rho}{\varepsilon}\left[\frac{\partial \boldsymbol{u}}{\partial t} + (\boldsymbol{u}.\nabla)\frac{\boldsymbol{u}}{\varepsilon}\right] = -\nabla p - \frac{\nabla.\bar{\bar{\tau}}}{\varepsilon} - \left(\frac{\mu}{K} + \beta_F|\boldsymbol{u}|\right)\boldsymbol{u} \tag{2}$$

$$\rho C_p\left[\varepsilon\frac{\partial T}{\partial t} + (\boldsymbol{u}.\nabla)T\right] = \nabla.(k\nabla T) + \frac{\bar{\bar{\tau}}.\nabla \boldsymbol{u}}{\varepsilon} + \varepsilon\frac{Dp}{Dt} - Nu\frac{k}{d_h}\, a_{sf}(T - T_s) \tag{3}$$

Where the viscous tensor, $\bar{\bar{\tau}}$ is defined by

$$\bar{\bar{\tau}} = (\mu)[\nabla \boldsymbol{u} + (\nabla \boldsymbol{u})^T] - \frac{2}{3}(\mu)(\nabla.\boldsymbol{u}) \tag{4}$$

The three last terms in Eq. (3), represent viscous dissipation, pressure work and non-equilibrium heat source, respectively.

Assuming the gas to be ideal, the state equation is,

$$\rho = p/RT \tag{5}$$

185 In the solid phase, the energy equation is

187 $$(1-\varepsilon)\rho_s C_{ps}\,\partial T_s/\partial t = \nabla.\left(\overline{\overline{k_e}}\nabla T_s\right) + Nu\frac{k}{d_h}a_{sf}(T-T_s) \quad (6)$$

186

188 Where, the solid effective thermal conductivity, $\overline{\overline{k_e}}$ is calculated based on volume average as,

189

190 $$\overline{\overline{k_e}} = k\,\varepsilon + (1-\varepsilon)k_s \quad (7)$$

191

192 **3.1 Permeability, Forchheimer Drag Coefficient and Nusselt number**

193 *3.1.1 Regenerator*

194 In the fluid momentum Eq. (2), the permeability, *K*, and Forchheimer drag coefficient, β_F can be evaluated for the

195 regenerator from the following one dimensional Darcy- Forchheimer and Darcy equations, respectively

196 $$\frac{\nabla p}{L} = \frac{\mu}{K}\,u + \beta_F\,u^2 \quad (8)$$

197 $$\frac{\nabla p}{L} = \frac{1}{2}\frac{f}{d_h}\,\rho\,u^2 \quad (9)$$

198 The friction-factor correlation for random fibre and its parameters (a_1, a_2, a_3) can be found in more details in [23].

200 $$f = \frac{a_1}{R_e} + a_2 {R_e}^{a_3} \quad (10)$$

199

201 Where Reynolds number,

202 $$R_e = \frac{\rho u d_h}{\mu} \quad (11)$$

203

204 The hydraulic diameter, d_h of a random fibre, in terms of porosity and wire diameter is determined by,

205

206 $$d_h = \frac{\varepsilon}{1-\varepsilon}d_w \quad (12)$$

207

Substituting the expression for friction-factor and the definition of Reynolds number into Eq. (9), and then equating the right-hand sides of equations Eq. (8) and Eq. (9), it can be determined that:

$$K = \frac{2{d_h}^2}{a_1} \tag{13}$$

$$\beta_F = \frac{1}{2d_h}\,\rho\,(a_2 {R_e}^{a_3}) \tag{14}$$

In energy Eq. (3) and (6), the Nusselt number, Nu and the solid surface area per unit volume, a_{sf} are calculated as

$$Nu = \left(1 + b_1 {P_e}^{b_2}\right) \tag{15}$$

$$a_{fs} = \frac{4\varepsilon}{d_h} \tag{16}$$

The correlation parameters (b_1, b_2) can be found in more details in [23].

3.1.2 Cooler

The velocity-pressure drop relationship for the cooler is obtained based on steady state simulation, as shown in Fig 3. The permeability, *K*, and Forchheimer drag coefficient, β_F are evaluated by fitting the data of velocity-pressure drop with Eq. (8) using the least square method. The permeability is found to be (9.87E-09 m^2) and the Forchheimer drag coefficient to be (293 kg/m^4). The average interstitial convective heat transfer coefficient, which is defined as the product of average heat transfer coefficient and the solid surface area per unit volume is found from simulation to be (1E+06 W/m^3. K).

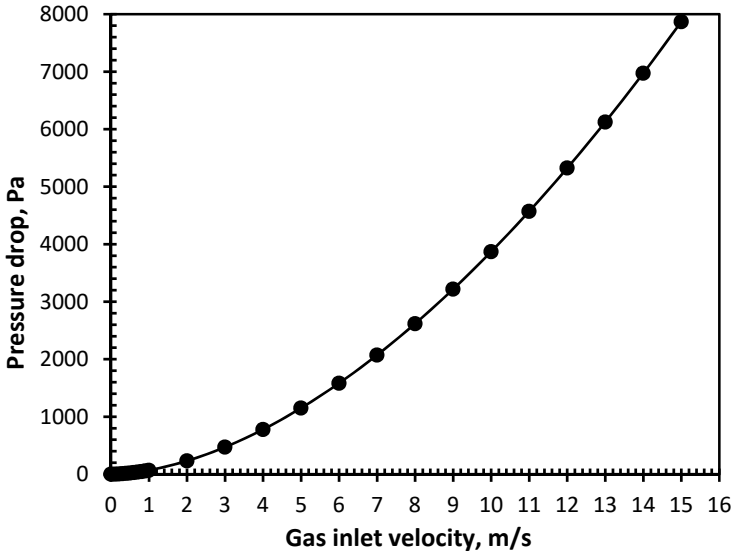

Fig. 3. Pressure drop through cooler using steady state simulation.

The indicated PV power, was collected and integrated over the total cycles using Simpson's rule, and calculated by:

$$\dot{W} = \left[\oint pdVdt\right]_{Exp} - \left[\oint pdVdt\right]_{Comp} \quad (17)$$

The coolant thermal power was calculated from the total heat output over the cooler surfaces over the cycles.

$$\dot{Q}_c = \left[\oint Qdt\right] \quad (18)$$

3.1.3 Boundary Conditions and Solution Scheme

The computational domain of the engine geometry is demonstrated in Fig.4. Moving and sliding walls are applied on the displacer and power pistons walls. The moving boundaries of the displacer and power pistons are predefined from equations of real motion of the pistons adopted from [24] as

$$Xe = r\left[1 - \cos\theta + \frac{1}{\lambda_e}\left(1 - \sqrt{1 - {\lambda_e}^2 \sin^2\theta}\right)\right] \quad [19]$$

$$Xc = r\left[1 - \cos(\theta - \pi/2) + \frac{1}{\lambda_c}\left(1 - \sqrt{1 - {\lambda_c}^2 \sin^2\left(\theta - \frac{\pi}{2}\right)}\right)\right] \quad [20]$$

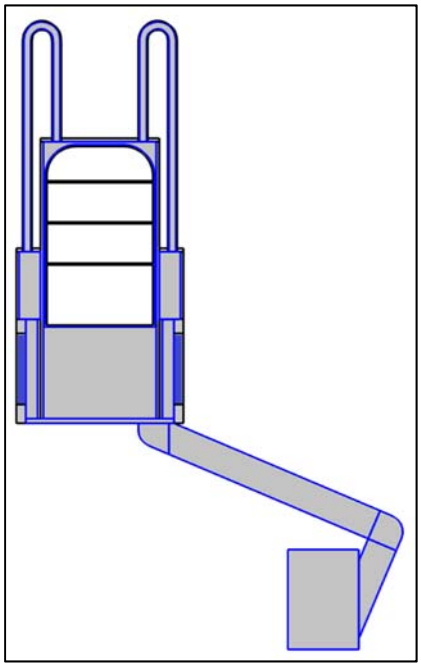

Fig. 4. The 2D computational domain of the engine.

Except constant temperature walls of heater and cooler, the other walls are treated as adiabatic walls. The unsteady time-dependent solution of the governing equations was initialized with steady state solution of heat transfer with no flow condition (no pistons motion). The computational time can be significantly reduced with the adoption of steady state solution as the temperature gradient is well established throughout the engine. The CFD model was set up with respect to the meshing size, time stepping and tolerances. Extremely fine triangular meshing was adopted in this study. The total number of elements are 39,000 with an average element quality of 0.9. The time stepping is resolved by 100 times over one cycle. All simulations are carried out on a PC with configuration of Intel(R) core(TM) CPU i7-4820K, runs at speed of 3.7 GHz with 48 GB RAM memory. Typically, each simulation run takes 2-3 days with normally 10 cycles to reach periodic steady state.

4. Model Validation

The indicated PV diagram predicted by the model was compared with experimental results at normal operating conditions as depicted in Fig. 5. It can be seen that the minimum and the maximum pressures predicted by the model are very close to experimental results. However, the gap areas in indicated PV diagrams between the model and experimental results are observed. This may be attributed to that the porous media characteristics obtained for the cooler using steady state simulation is underestimated. In such oscillatory flow environment of Stirling engine, the

pressure drop tends to be higher than steady flow [25]. In general, the maximum deviation in predicting the indicated power is 9% compared to experimental results.

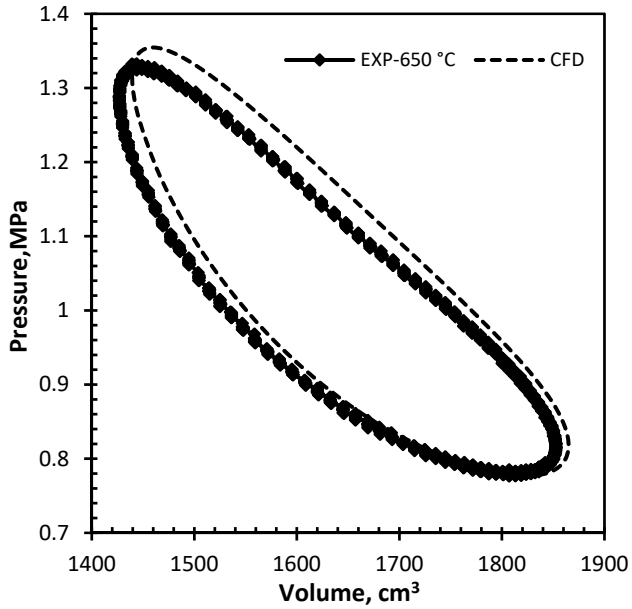

Fig. 5. Comparison of indicated PV diagrams between CFD model and experiment at normal operating conditions.

The effect of hot end temperature on engine indicated and cooling powers was investigated for further comparison between CFD model and experimental results. Five test runs were conducted, with a variation of hot end temperature from 450 °C to 650 °C, at nominal engine speed of 500 rpm and fixed charge pressure of 10 bar. As can be seen in Fig. 6, the CFD model results showed a similar increasing trend to experimental results of indicated and cooling powers with increasing the hot end temperature up to the maximum temperature of the heater with a maximum deviation of 9% and 5%, respectively.

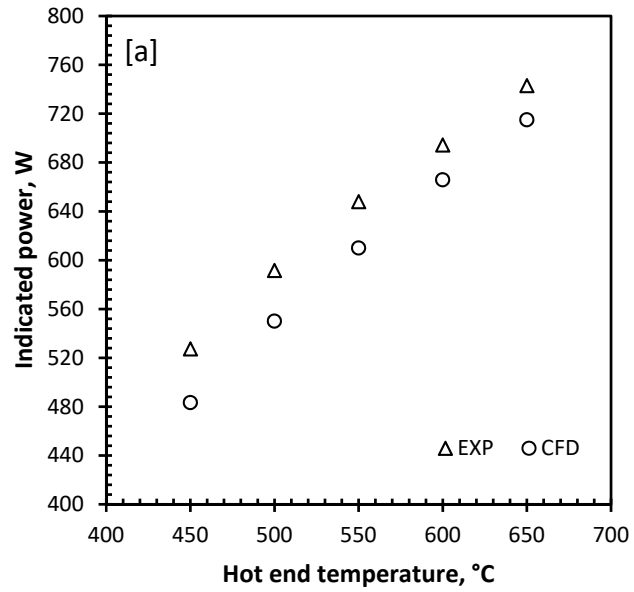

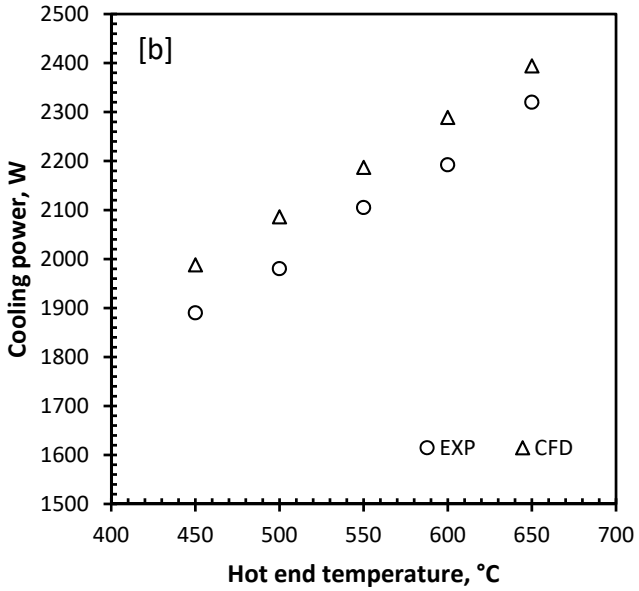

Fig. 6. Comparison between CFD model and experimental results at constant charge pressure (10 bar) and different heater temperature, (a) indicated power and (b) cooling power.

5. Results and discussion

In this section, some general results of the simulated engine are presented. The operational conditions of the engine were listed previously in table 1. The variation of total, expansion space, compression space volumes versus the crank angle is shown in Fig. 7. The compression ratio is the ratio of maximum to minimum total volumes, as read, 1850 cm^3 and 1425 cm^3, respectively. The compression space volume is that volume of the working gas confined between the top of power piston and the bottom of displacer piston. It follows that the maximum volume of the compression space is larger than that of the expansion space.

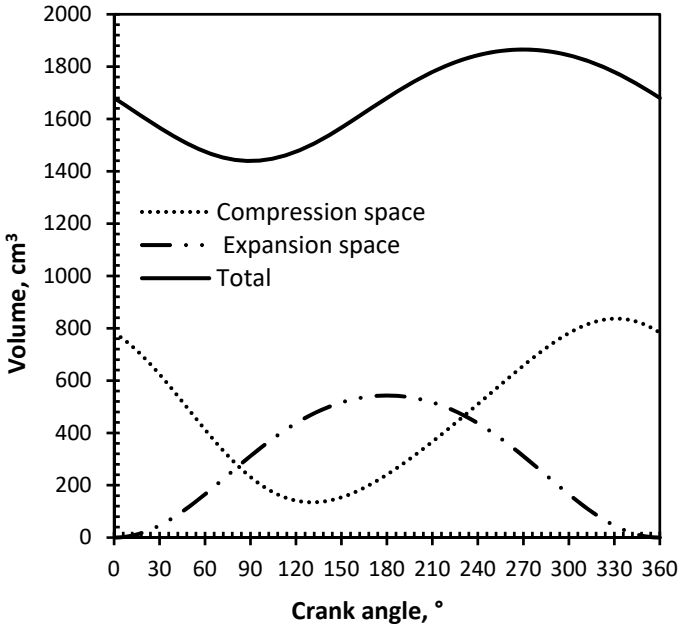

Fig. 7. Variation of total, expansion, compression volumes versus crank angle within an engine cycle.

The PV diagrams for compression and expansion spaces are illustrated in Fig. 8. It is noticeable that the positive expansion work is larger in magnitude than the negative compression work giving rise to the net output work from the engine.

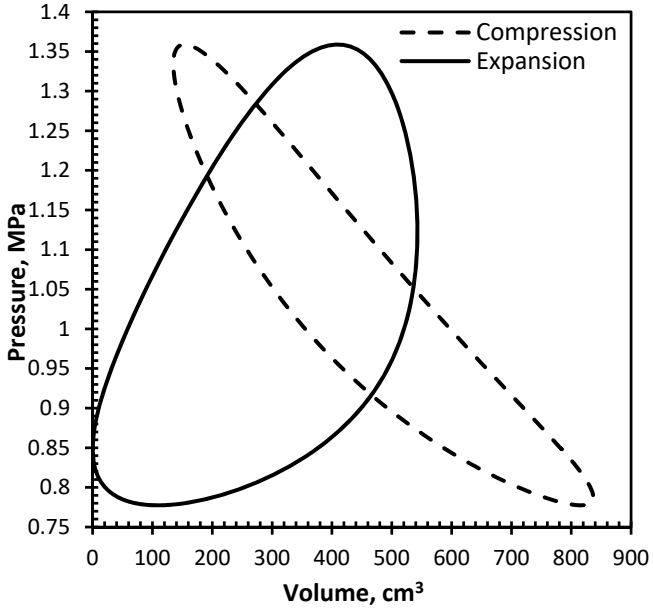

Fig. 8. PV diagrams for expansion and compression volumes within an engine cycle at 500 rpm.

The velocity, pressure and temperature contours are plotted in Fig. 9 at the end of the 5th cycle (t = 0.6s) at engine nominal speed. As can be seen that the engine has asymmetric geometry near the connecting pipe which affects the uniformity of fluid flow in the engine. Due to the combined motion of the power piston and displacer, gas moves forward and backward through engine domains. In Fig. 9(a), the gas flows from compression space through the

connecting pipe with an average velocity of (5m/s), where it splits into two streams due to asymmetric geometry. Part of the gas mass enters the cooler, meanwhile, the bulk flow is strongly jetting into the lower part of the expansion space causing flow vortexes as a result of jet impingement on the lower surface of the displacer. While, most of the gas is confined at the lower part of the engine, engine is cooled by a cooling water jacket. At this instant (t = 0.6s), as the power piston moves to the right and the displacer moves down, compression process takes place at the beginning of the new cycle and is completed when power piston reaches top dead centre (TDC), while displacer piston reaches bottom dead centre (BDC). Pressure gradient is established across the engine spaces giving rise to cyclic pressure during compression process as seen from Fig. 9(b). The maximum pressure drop normally occurs in the regenerator during the cycle due to the elevated inertia losses in the pore volumes of the matrix. The gas continues the thermodynamic cycle; heat is being supplied by the electric heater causing the gas to expand and more positive power is generated from the engine. The temperature contours of the gas phase across the engine spaces are shown in Fig. 9(c) with almost linear gradient across the engine spaces between hot and cold end temperatures. The gas coming from heater enters the regenerator, releases energy to the matrix and exits with a temperature normally higher than the cold end temperature. This depends on the regenerator effectiveness and thermal losses that occur in the regenerator. The higher thermal losses in the regenerator the higher cooling power is rejected from the engine. When the cooled gas is reversed during cold blow, the gas absorbs an amount of heat stored in regenerator matrix reducing the total amount of heat flow to the heater and hence boosting engine efficiency.

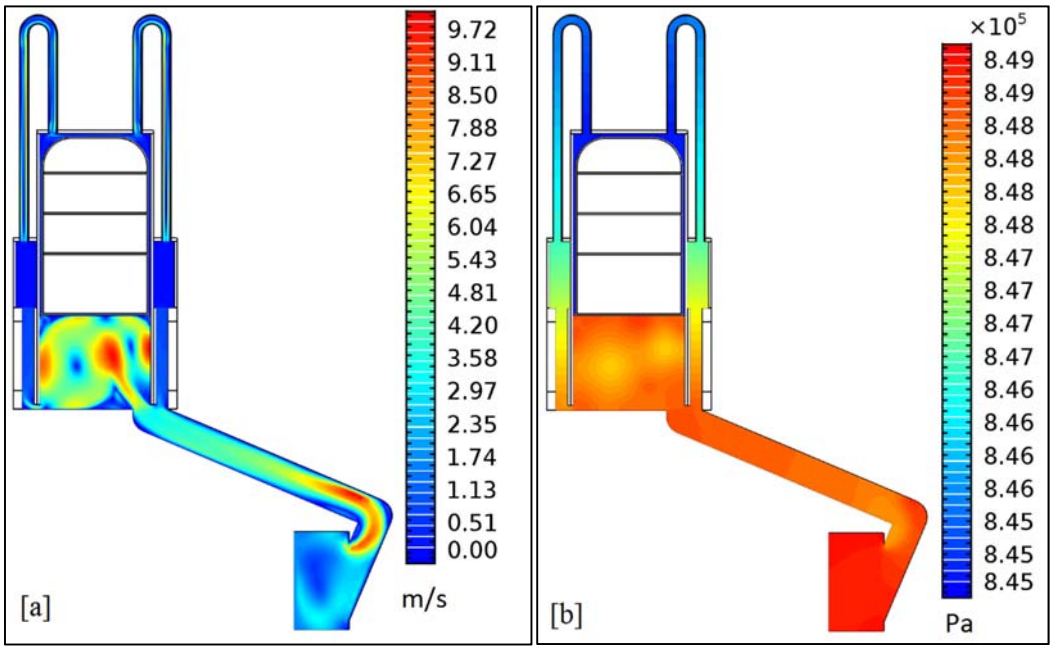

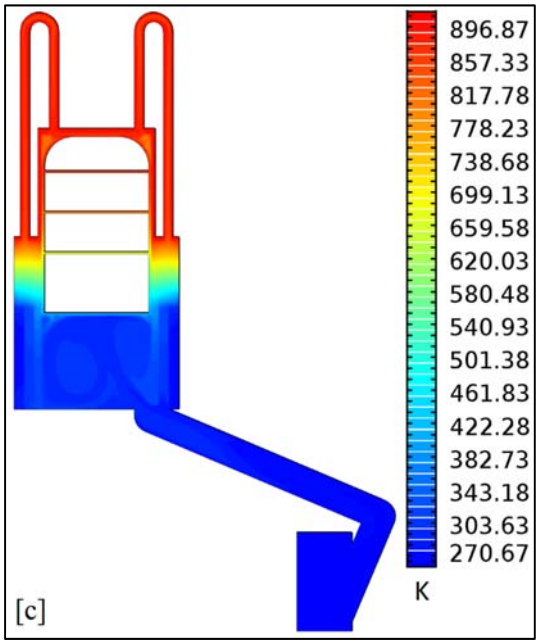

Fig. 9. CFD results during the 5th cycle (t = 0.6 s) at engine normal operating conditions, (a) velocity contour, (b) pressure contours, (c) temperature contours.

Fig. 10 shows the temperature contours in the two porous media (regenerator and cooler), respectively. The average regenerator matrix temperature was found to be 580K after a few cycles, which is slightly higher than the logarithmic mean temperature difference that is widely evaluated in second-order analysis as, $T_r = (T_h - T_k)/\ln(T_h/T_k)$ = 549K. It is worth noting that the connecting pipe is a two concentric pipes being cooled by the cooling water circuit but most of the heat is rejected from the main cooler.

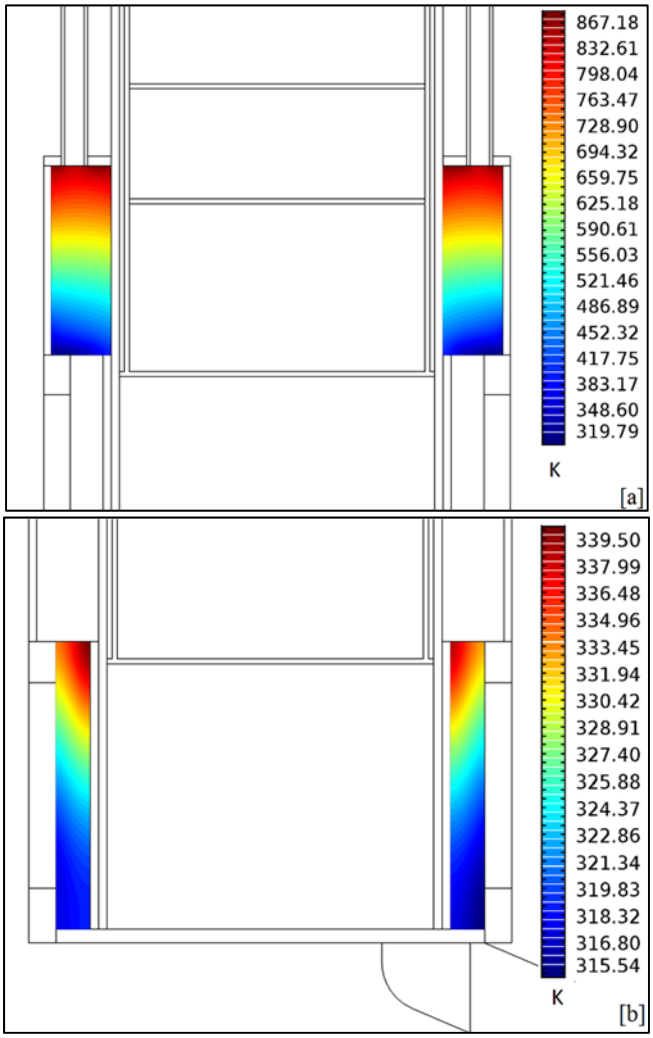

Fig. 10. Temperature contours of porous domains during the 5th cycle (t = 0.6 s) at engine normal operating conditions, (a) Regenerator, (b) Cooler.

The variation of Average-Weighted temperatures in different spaces of the engine, are shown in Fig. 11. The cyclic temperature variation is nearly sinusoidal except for heater tubes and cooler. For the expansion space temperature, the peak-to-peak magnitudes are nearly 923 K and 825 K, respectively. The maximum peak value occurs at crank angle of 90 °C. The compression space temperature fluctuates between 308 K and 270 K, respectively. Meanwhile, the regenerator cyclic temperature is nearly constant with an amplitude of 5 K. it is worth noting that the heat is supplied to the heater tube walls as well as the outer walls of the cylinder containing the displacer. This justifies that the temperature variation of the gas in expansion space, between nearly phase angles [50° 200°], is showing higher values than that of heater tubes.

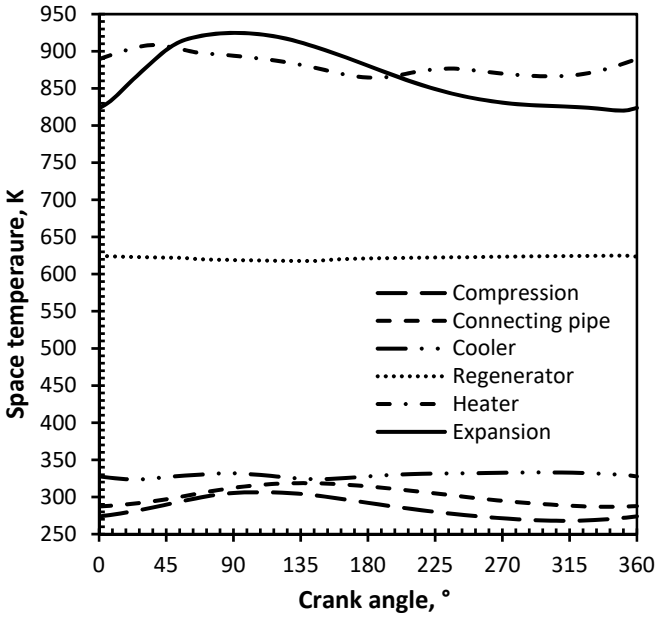

Fig. 11. Spaces cyclic temperatures vs. crank angle during the 5th cycle at engine normal operating conditions.

It is a common understanding that maximum power output is obtained at a phase angle of 90°. In fact, most gamma-type Stirling engines with standard crank mechanism are phased out with 90° for practical reasons and not because of its optimal thermodynamic behaviour. On the other hand, variation of phase angle was acknowledged as one of the best ways for controlling Stirling engine power. As a result of phase angle choice, three major effects on engine parameters are expected; it influences the pressure amplitude, the total volumetric change of the gas, and heat transfer and hence engine indicated power. The total volume variation with phase angle shown in Fig. 12, indicates that the maximum and the minimum volumes are unchanged. However, there is a shift of angles at which minimum and maximum volumes normally occur. At phase angle of 120°, large volume variation is observed during compression process starting from 1769 cm^3 to 1429 cm^3. On the other hand, at lower phase angle of 60°, compression volume varies from 1556 cm^3 to 1429 cm^3.

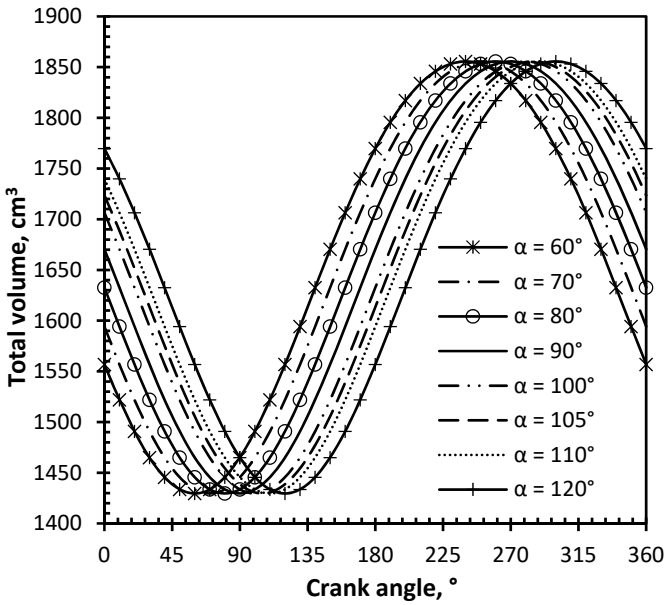

Fig. 12. Total volume vs. crank angle at different phase angles.

The effect of phase angle variation on cyclic pressure drop across the regenerator is shown in Fig. 13. For all phase angles shown, it can be seen that the pressure loss variation is sinusoidal. Though, peak-to-peak values of pressure loss exhibit different values during the hot and cold blow times of the cycle. This may be attributed to differences of gas properties and gas velocities as such higher gas volumetric is exchanged during the hot blow by the movement of the relatively larger displacer. For the standard case of 90° phase angle, the maximum pressure drop in the regenerator reaches 0.31 bar, with maximum charge pressure of 10 bar. As the phase angle increases from 60° to 120°, the maximum pressure drop increases from 0.19 bar reaching 0.42 bar. There is almost a shift of 10° at which minimum and maximum pressure drop normally occurs. At any given combination of operating condition, there would be a balance between the favourable increased heat transfer rate and the elevated pressure drop and hence the optimum value for engine performance parameter is achieved.

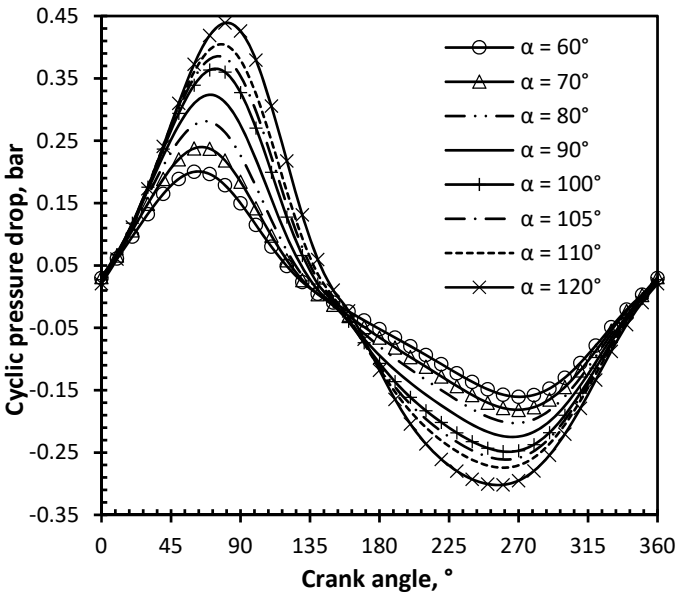

Fig. 13. Pressure drop across the regenerator vs. crank angle at different phase angles.

The effect of phase angle on indicated PV diagrams is demonstrated in Fig. 14. It can be seen that the lager phase angles the higher pressure amplitude. The pressure amplitude is most likely a result of temperature variation rather than the gas compression. It is worth noting that a maximum indicated power was found to be 750 W at a phase angle of 105°. This obtained optimum phase angle agrees closely with the results found in [26]. While a minimum value was found to be 440 W at a phase angle of 60°. The indicated power generated at a phase angle of 90° is 714 W, which is 5% lower than that at 105°. This deviation could be more pronounced at higher engine frequencies [27]. The optimum value of indicated power is most likely a result of balance between the negative effect of pressure drop (specifically, across the regenerator) and the positive effects caused by the increase in heat transfer rate due to the increased volumetric gas exchange, compression and pressure ratios. The indicated power and power loss due to pressure drop in the regenerator are presented in Fig.15 at different phase angles. The indicated power loss is calculated based on the difference between indicated power at each phase angle to the indicated power at optimum phase angle of 105°.

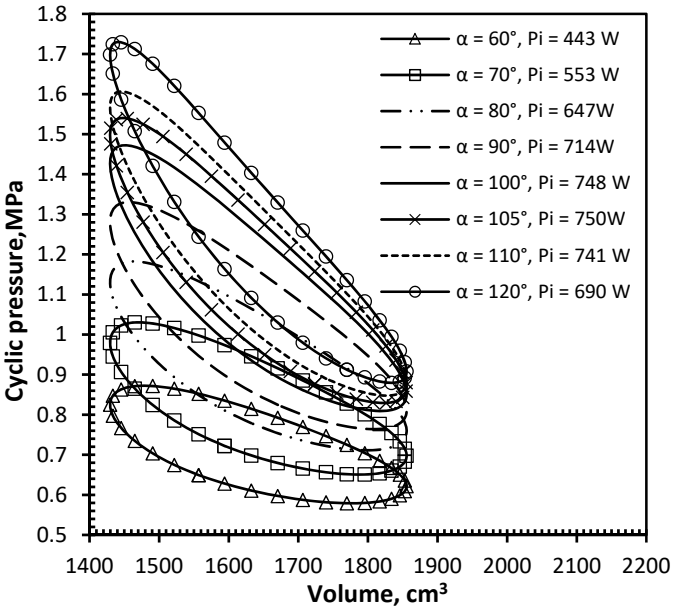

Fig. 14. Indicated PV diagrams at different phase angles.

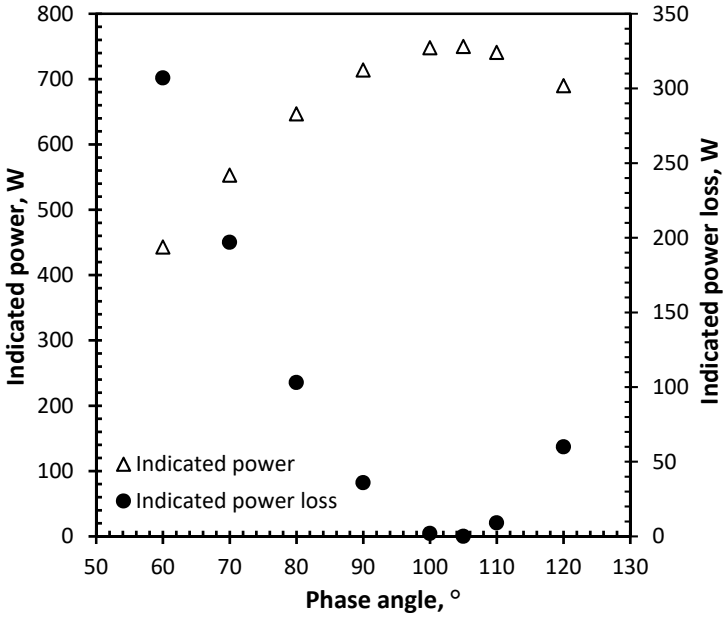

Fig. 15. Indicated power and indicated power loss at different phase angles.

Realizing that dead space is harmful to Stirling engine leads to Finkelstein' generalization [28]; 'harmful dead space to be minimized'. In theory, this unswept volume should be kept minimum which contradicts with real engines that can have up to 50% dead volume of its total gas volume. A closer inspection to the current engine indicates that the connecting pipe which connects the compression space and the lower part of the expansion space, is relatively large compared to other dead spaces of the engine (heat exchangers). The reduction of connecting pipe diameter, and hence the dead volume, can be achieved without alteration of the general layout of the engine, using a reduced pipe

and two adaptors as geometrically depicted in Fig. 16. The recirculation and vortex separation of velocity streamlines is strongly pronounced in the original pipe compared to the suggested reduced pipe.

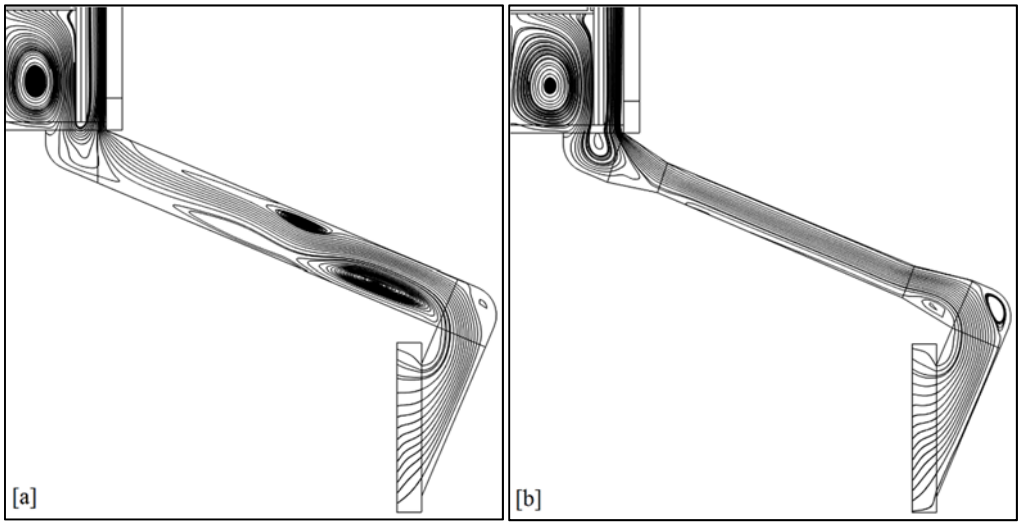

Fig. 16. Effect of connecting pipe diameter on velocity streamlines during the 5th cycle (a) original pipe and (b) reduced pipe.

With reducing the pipe diameter from 30 mm to 12 mm, its effect on engine performance can be seen in Fig. 17. The indicated power (Fig 17(a)) increases until reaching a maximum value of 887 W at pipe diameter of 14 mm and then falls down. This may be attributed to the increased pressure ratio as dead volume decreases. At lower values of pipe diameter, the pressure in the pipe increases which means that more resistance the displacer experiences when it moves down during compression process. Therefore, more useful power is consumed to overcome this resistance and the net indicated power drops down. On the other hand, the cooling power (Fig 17(b)) is showing an increasing trend with reducing the connecting pipe diameter.

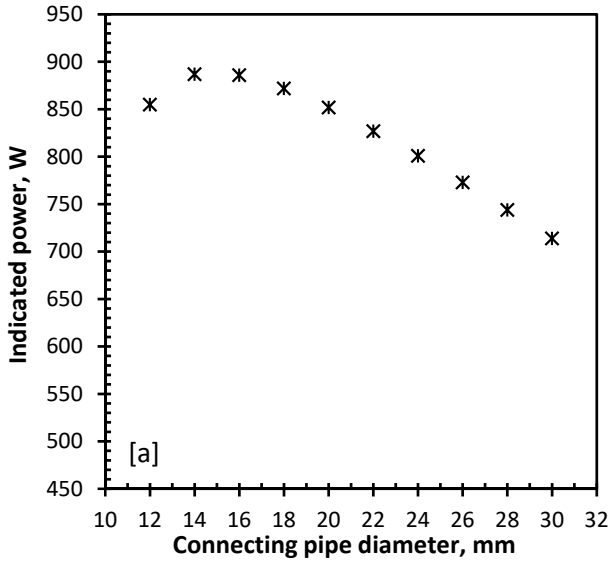

409

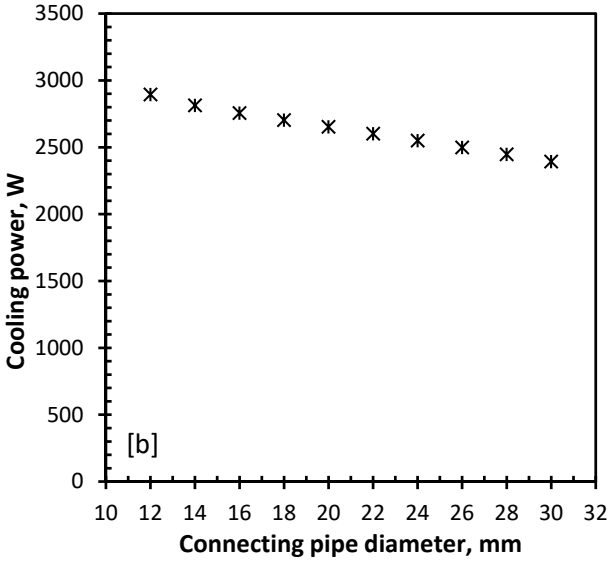

410

411 **Fig. 17.** Effect of connecting pipe diameter on engine performance, (a) indicated power and (b) cooling power.
412
413
414 **6. Conclusion**

415 A comprehensive 2D CFD model of gamma-type Stirling engine was developed and validated to investigate the
416 effect of phase angle and dead volume variations on engine performance. The results revealed that phase angle
417 variation poses significant impact on engine indicated power. Power increases as phase angle increases up to an
418 optimum value then it falls down. The optimum value exists as a result of balance between increased gas volumetric
419 exchange and compression ratio, and the elevated pressure drop in the regenerator. the optimum phase angle was
420 found to be 105° rather than the common phase angle of 90°. the dead volume (connecting pipe) is observed to pose
421 negative effects on engine indicated power and therefore, an optimum value of pipe diameter exists and found to be

14 mm. The CFD model is maturing and will be extended for 3D simulations for better understanding of fluid flow and heat transfer characteristics inside the engine.

References

[1] Goswami DY, Kreith F, editors. Handbook of energy efficiency and renewable energy. CRC Press; 2007.

[2] Organ, AJ. The air engine: Stirling cycle power for a sustainable future. Elsevier, 2007.

[3] Ibrahim MB, Tew RC. Stirling convertor regenerators. CRC Press; 2011.

[4] Walker G. Stirling engines. Oxford University Press; 1980.

[5] Dyson RW, Wilson SD, Tew RC. Review of computational Stirling analysis methods. In Collect. Tech. Pap. Int. Energy Convers. Eng. Conference 2004; Vol. 1, pp. 511-531.

[6] Wilson D, Dyson R, Tew R, and Ibrahim M, Multi-D CFD modelling of a free-piston Stirling convertor at NASA GRC, In Proceedings, 2nd International Energy Conversion Engineering Conference, AIAA, 2004, Vol. 5673.

[7] Ibrahim, MB, Zhang Z, Kembhavi S, A 2-D Axi-symmetric CFD model of oscillating flow with separation, International Energy Conversion and Engineering Conference, Paper No. 20121, 2002.

[8] Bert J, Chrenko D, Sophy T, Le Moyne L, Sirot F. Simulation, experimental validation and kinematic optimization of a Stirling engine using air and helium. Energy. 2014; 78:701-712.

[9] Chen WL, Wong KL, Chen HE. An experimental study on the performance of the moving regenerator for a γ-type twin power piston Stirling engine. Energy Conversion and Management. 2014; 77:118-128.

[10] Hooshang M, Moghadam RA, Nia SA, Masouleh MT. Optimization of Stirling engine design parameters using neural networks. Renewable Energy. 2015; 74:855-866.

[11] Hachem H, Gheith R, Aloui F, Nasrallah SB. Numerical characterization of a γ-Stirling engine considering losses and interaction between functioning parameters. Energy Conversion and Management. 2015; 96:532-543.

[12] Araoz JA, Cardozo E, Salomon M, Alejo L, Fransson TH. Development and validation of a thermodynamic model for the performance analysis of a gamma Stirling engine prototype. Applied Thermal Engineering. 2015; 83:16-30.

[13] Gheith R, Aloui F, Nasrallah SB. Determination of adequate regenerator for a Gamma-type Stirling engine. Applied Energy. 2015; 139:272-280.

451 [14] Li R, Grosu L, Queiros-Condé D. Losses effect on the performance of a Gamma type Stirling engine.
452 Energy Conversion and Management. 2016; 114:28-37.
453 [15] Mahkamov K. Design improvements to a biomass Stirling engine using mathematical analysis and 3D CFD
454 modelling. Journal of Energy Resources Technology. 2006;128(3):203-215.
455 [16] Chen WL, Wong KL, Chang YF. A computational fluid dynamics study on the heat transfer characteristics
456 of the working cycle of a low-temperature-differential γ-type Stirling engine. International Journal of Heat
457 and Mass Transfer. 2014; 75:145-155.
458 [17] Chen WL, Yang YC, Salazar JL. A CFD parametric study on the performance of a low-temperature
459 differential gamma-type Stirling engine. Energy Conversion and Management. 2015; 106:635-643.
460 [18] Hooshang M, Moghadam RA, AlizadehNia S. Dynamic response simulation and experiment for gamma-
461 type Stirling engine. Renewable Energy. 2016; 86:192-205.
462 [19] Ve-ingenieure. Datasheet of ST05-CNC Striling engine. online [Accessed on 10/04/2016]: http://ve-
463 ingenieure.de/projekt_st05g_cnc_engl.html
464 [20] Moffat RJ. Describing the uncertainties in experimental results. Experimental Thermal and Fluid Science
465 1988;1(1):3-17.
466 [21] COMSOL AB, COMSOL Multiphysics reference manual, Version 5.2, 2015.
467 [22] Tew R, Simon T, Gedeon D, Ibrahim M, Rong W. An initial non-equilibrium porous-media model for CFD
468 simulation of Stirling regenerators, In Proceedings of the 4th International Energy Conversion Engineering
469 Conference, 2006, Vol.1.
470 [23] Gedeon D, Wood JG. Oscillating-flow regenerator test rig: hardware and theory with derived correlations
471 for screens and felts; 1996.
472 [24] Wagner A. Calculations and experiments on gamma-type Stirling engines. Cardiff University; 2008.
473 [25] Organ AJ. Back to back test for determining the pumping losses in Stirling cycle machine. Proceedings of
474 the 17th intersociety energy conversion engineering conference, 1982. p. 1856–1861.
475 [26] Cheng CH, Yang HS. Optimization of geometrical parameters for Stirling engines based on theoretical
476 analysis. Applied energy. 2012 Apr 30; 92:395-405.
477 [27] Hoegel B, Pons D, Gschwendtner M, Tucker A, Sellier M. Thermodynamic peculiarities of alpha-type
478 Stirling engines for low-temperature difference power generation: Optimisation of operating parameters
479 and heat exchangers using a third-order model. Proceedings of the Institution of Mechanical Engineers,
480 Part C: Journal of Mechanical Engineering Science. 2014;228(11):1936-1947.

481 [28] Finkelstein T, Organ AJ. Air Engines. 2001, Professional Engineering Publishing, London and Bury St.
482 Edmunds.